Transition between Hall-Petch and inverse Hall-Petch behavior in nanocrystalline silicon carbide

Saeed Zare Chavoshi,[1,*] Paulo S. Branicio,[2] and Qi An[3]
[1]*Department of Materials, University of Oxford, Parks Road, Oxford OX1 3PH, United Kingdom*
[2]*Mork Family Department of Chemical Engineering and Materials Science, University of Southern California, Los Angeles, California 90089, USA*
[3]*Department of Chemical and Materials Engineering, University of Nevada-Reno, Reno, Nevada 89557, USA*

(Received 16 March 2021; revised 14 June 2021; accepted 8 July 2021; published 27 July 2021)

Despite much experimental and simulation effort, the existence of a Hall-Petch to inverse Hall-Petch transition in nanocrystalline ceramics remains elusive. By employing molecular dynamics simulations, we unambiguously reveal a transition from strengthening to softening in the shear deformation of nanocrystalline silicon carbide ceramics as a function of grain size. Results show a well-defined maximum in the shear strength for grain sizes in the range 6.2 to 7.7 nm. Further decrease in grain size leads to diminishing strength, consistent with an inverse Hall-Petch behavior. As grain size is reduced the increasing grain boundary (GB) regions lead to homogenization of shear stresses across the microstructure, allowing for lower local shear stress levels at higher macroscopically applied stresses. This delays shear localization within GB regions, preventing cavitation, nanocracking, and premature failure, and is responsible for the observed Hall-Petch behavior. In contrast, at grain sizes <6.2 nm, the rather compliant nature of the structurally disordered GB regions dominates the mechanical response, reducing the shear strength and triggering a transition into the inverse Hall-Petch behavior. A composite model delineating the transition between Hall-Petch and inverse Hall-Petch behavior is successful at describing the mechanical behavior of nanocrystalline silicon carbide as a function of grain size.

DOI: 10.1103/PhysRevMaterials.5.073606

I. INTRODUCTION

Nanocrystalline materials, comprising nanometer size grains, exhibit extraordinary mechanical properties, particularly high strength [1]. The dependence of the displayed strength as a function of grain size has been successfully described by the empirical Hall-Petch and inverse Hall-Petch relationships. Strengthening is induced by dislocation blockage effects, while softening is triggered by dislocation emission from grain boundaries (GBs) and activation of GB deformation mechanisms, such as grain rotation and GB sliding at very fine grain sizes [2–6]. In contrast, in ceramics, due to the nature of their chemical bonding, i.e., strong covalent or ionic bonding, and the crystal structure complexity, dislocation nucleation and motion at ambient temperature are significantly restricted. Hence, while Hall-Petch-like behavior has been observed in ceramics, the physically based explanations for the Hall-Petch relationship in metals, e.g., dislocation pile-up, are not directly applicable to justify their mechanical behavior as a function of grain size [7–12]. Although dislocation-based strain accommodation in some ceramics, e.g., strontium titanate ($SrTiO_3$) single crystal [13,14], hafnium diboride (HfB_2), and zirconium diboride (ZrB_2) polycrystals [15], at room temperature has been observed, that cannot explain the strengthening in other ceramics.

During the last few years, several experiments [16–22] and atomistic simulations [23–29] on nanocrystalline ceramics have demonstrated that grain size reduction <100 nm can induce contrasting effects on their mechanical properties. Both strengthening and softening have been reported, yet the detailed nanoscale mechanisms responsible for the displayed nanosized effects remain controversial. For example, recent experiments demonstrated that the hardness of nanocrystalline magnesium aluminate spinel ceramics ($MgAl_2O_4$) increases for grain size reduction down to grain sizes of 30 nm [17], 28 nm [18], 18.4 nm [19], and 7.1 nm [20], implying a Hall-Petch relationship. In contrast, hardness was reported to diminish for grain sizes 30 to 17.2 nm [17] and 18.4 to 5 nm [19], implying an inverse Hall-Petch behavior. For nanocrystalline MgO, the breakdown of the Hall-Petch behavior was reported to occur at a critical grain size of 130 nm [21]. Due to their complex structures as compared with metals, GBs in ceramics often form structurally disordered structures that can be described as an amorphous film of a composition-dependent thickness. Hardness increase in $MgAl_2O_4$ down to grain size of 7.1 nm was first attributed to the increase of the volume fraction of disordered GB regions; arguably, the strengthening was linked to cation site inversion increasing the average bond density and strength within GBs [20]. In contrast, inverse Hall-Petch behavior for $MgAl_2O_4$ from a critical grain size of 30 nm was linked to the increasing GB volume fraction, arguably weaker than the crystalline grains [17]. In nanocrystalline ceramics with grains of ∼30 nm and an average GB thickness of ∼2 nm, the total volume fraction of GBs is ∼20% [30,31]. The GB fraction increases sharply for smaller grain sizes, e.g., for $MgAl_2O_4$ with 7.1 nm grain size, it was reported to be as high as 60% [20]. Thus, this colossal fraction of "weaker" regions should certainly

*Corresponding author: saeed.zarechavoshi@materials.ox.ac.uk

affect the mechanical properties of the material [17]. In agreement with this understanding, other studies reported inverse Hall-Petch behavior in $MgAl_2O_4$ and MgO, correlating with increasing GB volume fraction and triple junctions as grain size is reduced [19,21].

Other ceramics also display distinct mechanical behavior when grains are reduced to nanodimensions. Nanocrystalline silicon carbide (SiC) was reported to deform superplastically at a grain size of 200 nm; nonetheless, the tensile loading testing was performed at high temperature [22]. Recent molecular dynamics (MD) simulations indicated an inverse Hall-Petch behavior for nanocrystalline SiC at grain sizes ranging from 16 to 4 nm [23] and 3.5 to 0.9 nm [24]. The behavior was linked to reduced number of intact Si-C bonds and increased volume fractions of the soft amorphous GB phase with grain refinement. Reduced tensile yield stress accompanied by enhanced toughness was also reported for nanocrystalline SiC with grain size reduction from 20 to 3 nm [25]. MD simulations also revealed that nanocrystalline SiC can show superplastic deformation at room temperature as grain sizes are reduced to 2 nm, which was associated with the large GB and triple junction volume fractions in the samples at such small grain size [26]. A crossover from intergranular continuous deformation to intragrain discrete deformation arising from the interplay between cooperative GB sliding, grain rotations, and intergranular dislocation formation was reported for nanocrystalline SiC under indentation loading, leading to a transition from deformation dominated by indentation-induced crystallization to deformation dominated by disordering and amorphization [27]. Inverse Hall-Petch behavior was also observed in simulations of shear deformation of nanocrystalline boron carbide (B_4C) with grain sizes ranging from 14.6 to 4.8 nm, where GB sliding and amorphization processes were reported to be the dominant deformation mechanisms [28].

To shed light on the contrasting Hall-Petch-like behavior reported for nanocrystalline ceramics and the underlying deformation mechanisms, we performed MD simulations of shear deformation in nanocrystalline silicon carbide (3*C*-SiC) of varying grain sizes from 18.6 to 3.7 nm. Due to the technological importance of 3*C*-SiC ceramics [32–34], it is critical to understand how such nanocrystalline material behaves under shear loading, what the dominating deformation mechanisms are, and whether a Hall-Petch to inverse Hall-Petch-like transition occurs for decreasing grain size. The results indicate an unquestionable transition from Hall-Petch to inverse Hall-Petch behavior at a critical grain size of ∼7 nm. Such a transition is defined by the competition between strengthening induced by GB shear stress homogenization and softening induced by the increasing GB volume and GB deformation mechanisms.

II. METHODOLOGY

A. Shear response of nanocrystalline samples

MD simulations were performed using the LAMMPS package [35] with the effective many-body interatomic potential for SiC developed by Vashishta *et al.* [36]. The potential was validated by reproducing the generalized stacking fault energies, cohesive energy, elastic constants, and melting temperature of 3*C*-SiC [36]. This potential has been successfully used to describe the behavior of SiC under shock loading [37–43], the dynamic deformation of SiC nanowires [44], SiC dynamic fracture [45], as well as the properties of SiC in the amorphous phase [46]. Various three-dimensional (3D) nanocrystalline samples were generated using the Poisson-Voronoi tessellation method [47]. All systems were composed of 125 randomly oriented grains with average grain sizes from 3.7 to 18.6 nm, containing 325 686 to 40 722 382 atoms. An example of the 3D nanocrystalline 3*C*-SiC structure (18.6 nm average grain size) along with its grain size distribution is illustrated in Figs. 1(a)–1(c). Atoms in Fig. 1(b) are colored according to a structure identification algorithm for the diamond structure [48] to characterize crystalline intragranular and disordered intergranular configurations. Grain size distributions for all samples are provided in Fig. S1 in the Supplementary Material [49]. Periodic boundary conditions were applied along all three directions to eliminate surface effects. The Velocity-Verlet algorithm with a time step of 1.0 fs was used to integrate the equations of motion. Each sample was first relaxed using a conjugate gradient energy minimization, which was followed by a high-temperature annealing at $T = 2000$ K and $P = 0$ GPa for 30 ps using the isothermal-isobaric (NPT) ensemble. The samples were then cooled down to room temperature and subsequently equilibrated at $T = 300$ K for 10 ps. Finally, using constant temperature simulations, a homogeneous shear deformation was applied in the xy plane at a constant engineering strain rate of $10^9\ s^{-1}$ up to a total shear strain of 0.15.

B. Shear response of crystalline and disordered phases

Three periodic 3D monocrystalline 3*C*-SiC structures with cubic length size of 25 nm (1 474 560 atoms) were generated with independent crystal orientations. The sample crystal structure directions [100], [010], [001]; [110], [$\bar{1}$10], [001]; and [11$\bar{2}$], [111], [$\bar{1}$10] were aligned along the x, y, and z simulation box axes, respectively. The samples were relaxed and thermalized as described for the nanocrystalline samples. As a final step, using constant temperature simulations, a homogeneous shear strain loading at a constant shear rate of $10^9\ s^{-1}$ was imposed along the xy, xz, and yz planes. To obtain an amorphous configuration, an initial monocrystalline sample was melted and thermalized at 4000 K for 20 ps and subsequently quenched from 4000 to 300 K in 20 ps. Finally, the amorphous sample was thermalized at 300 K for 10 ps.

C. Analysis tools

The shear localization parameter (Ψ) was used to quantify the degree of localization in the nanocrystalline samples $\Psi = \sqrt{\frac{1}{N}\sum_{i=1}^{N}(\eta_i^{\text{Mises}} - \bar{\eta}^{\text{Mises}})^2}$, with $\bar{\eta}^{\text{Mises}} = \sum_{i=1}^{N}\eta_i^{\text{Mises}}/N$, where η_i^{Mises} and N are the von Mises atomic shear strain and the number of atoms in the system, respectively [50–52]. Total GB energies (E_{GB}) were calculated based on the differential total system energy of nanocrystalline samples (E_{NC}) and their single crystalline counterparts (E_{SC}) over the GB surface area (A_{GB}) obtained by a surface mesh technique [53] $E_{\text{GB}} = (E_{\text{NC}} - E_{\text{SC}})/A_{\text{GB}}$. To calculate the

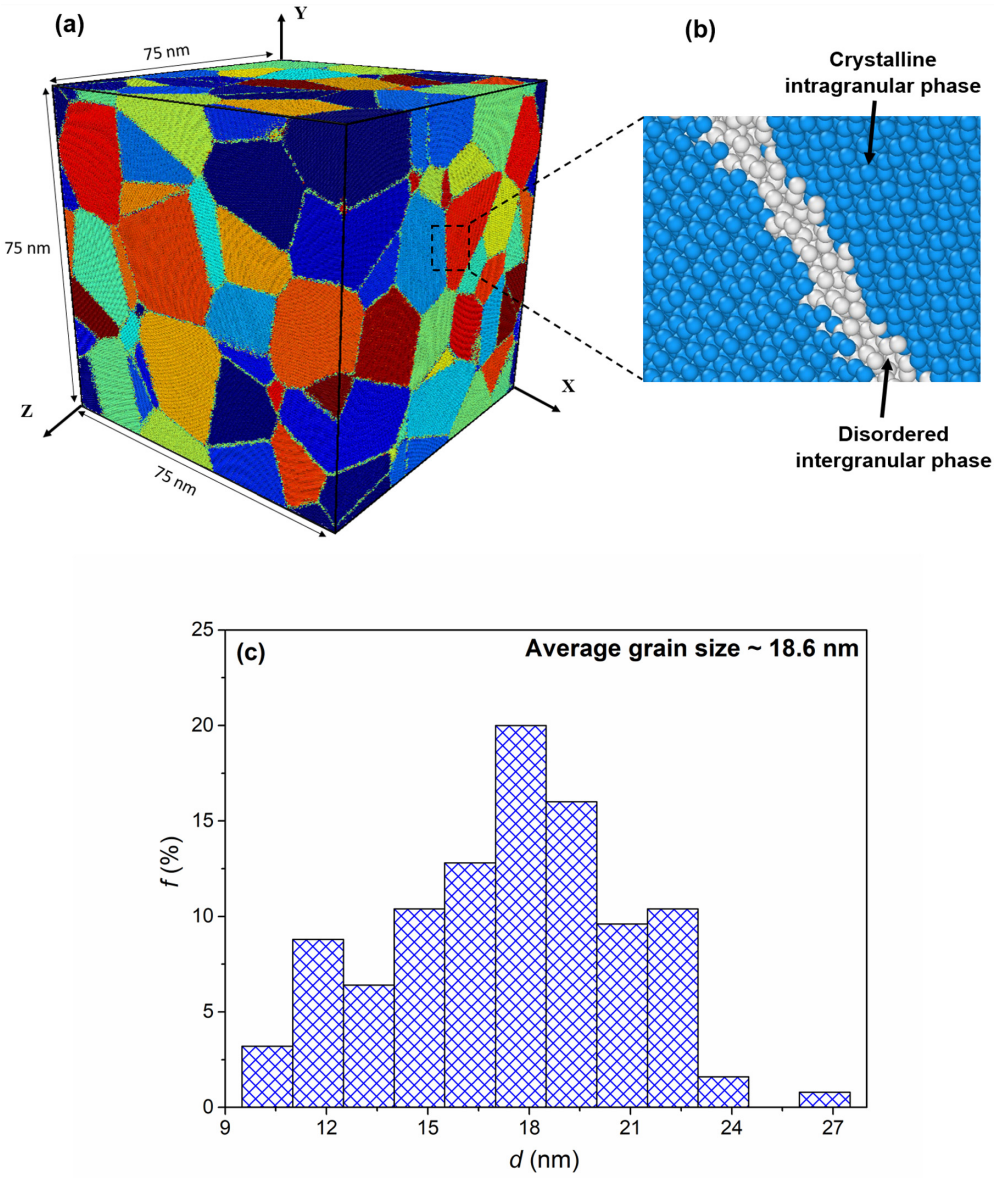

FIG. 1. (a) Illustration of the nanocrystalline 3*C*-SiC structure with average grain size of 18.6 nm after relaxation. Grains are depicted in different colors. (b) Crystalline intragranular (pristine zinc blende structure) and disordered intergranular phases shown in blue and gray, respectively. (c) Grain size distribution of the sample shown in (a).

volume fraction of the crystalline and structurally disordered phases, a structure identification algorithm for the diamond lattice [48] was utilized, where atoms in local zinc blende structure were identified as belonging to grains, while others to GBs.

III. RESULTS AND DISCUSSION

From the shear deformation simulations of the various nanocrystalline 3*C*-SiC samples, with average grain sizes from 3.7 to 18.6 nm, we calculated the shear stress-strain response, which is shown in Fig. 2(a). The curves display a well-defined grain size dependence of the shear modulus, yield strain, and shear strength. For comparison, Fig. 2(b) shows a plot of the calculated shear strength vs yield shear strain for the seven systems investigated. Here, the *shear strength* is defined as the peak stress on the shear stress-strain curve before stress drop, and the corresponding *shear strain* is defined as the yield shear strain. Samples with the grain sizes 7.7 and 6.2 nm exhibit the highest shear strength at ∼6.5 GPa. The shear yield strains are in the range of ∼0.07–0.12 and increase for decreasing grain size, which can be associated with the increasing volume fraction of softer amorphous phases within GBs, see Fig. 3(b). To check the reproducibility of the results, the simulations were repeated for selected grain sizes ranging from ∼7.7 to 3.7 nm using new samples generated by Voronoi tessellation, and nearly the same trend was observed, see Fig. S2 in the Supplementary Material [49]. Figure 1(b) demonstrates two coexisting phases in the nanocrystalline 3*C*-SiC, i.e., crystalline intragranular

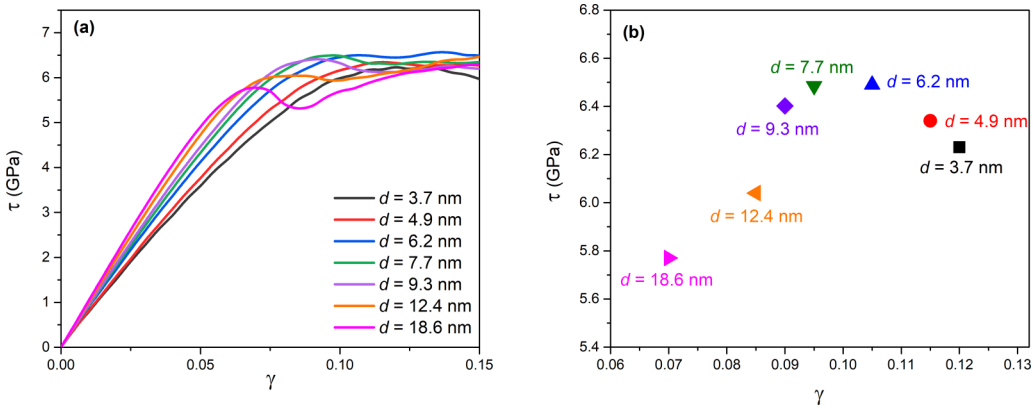

FIG. 2. (a) Shear response of various nanocrystalline 3*C*-SiC systems with different grain sizes. (b) Shear strength (τ) vs critical shear strain (γ).

(in blue) having intact strong Si-C covalent bonds and disordered intergranular (in gray) phases [27]. The soft disordered phase within GBs could control the plasticity and trigger a rather homogenous deformation in finer grain size samples, leading to higher failure strains. This is consistent with the observed superplastic tensile behavior of very fine-grained nanocrystalline SiC [26].

Variations in shear strength and shear modulus with grain size are plotted in Fig. 3(a), where three distinct regions can be identified: (I) sharp increase of shear strength to ~6.4 GPa down to grain size of 9.3 nm; (II) plateauing of the strengthening effect for grain sizes between 6.2 and 9.3 nm. Within this region, the shear strength reaches its maximum ~6.5 GPa; (III) steady decrease of shear strength for grain sizes <6.2 nm. Accordingly, a Hall-Petch-like behavior can be identified in regions (I) and (II), whereas region (III) represents an inverse Hall-Petch-like regime. The simulation results indicate that the maximum shear strength for the nanocrystalline 3*C*-SiC occurs at grain sizes in the range of 6.2 to 7.7 nm. Possible explanations for this observation can be traced to shear localization processes combined with GB energies and crystalline volume fraction of the samples. Recent studies

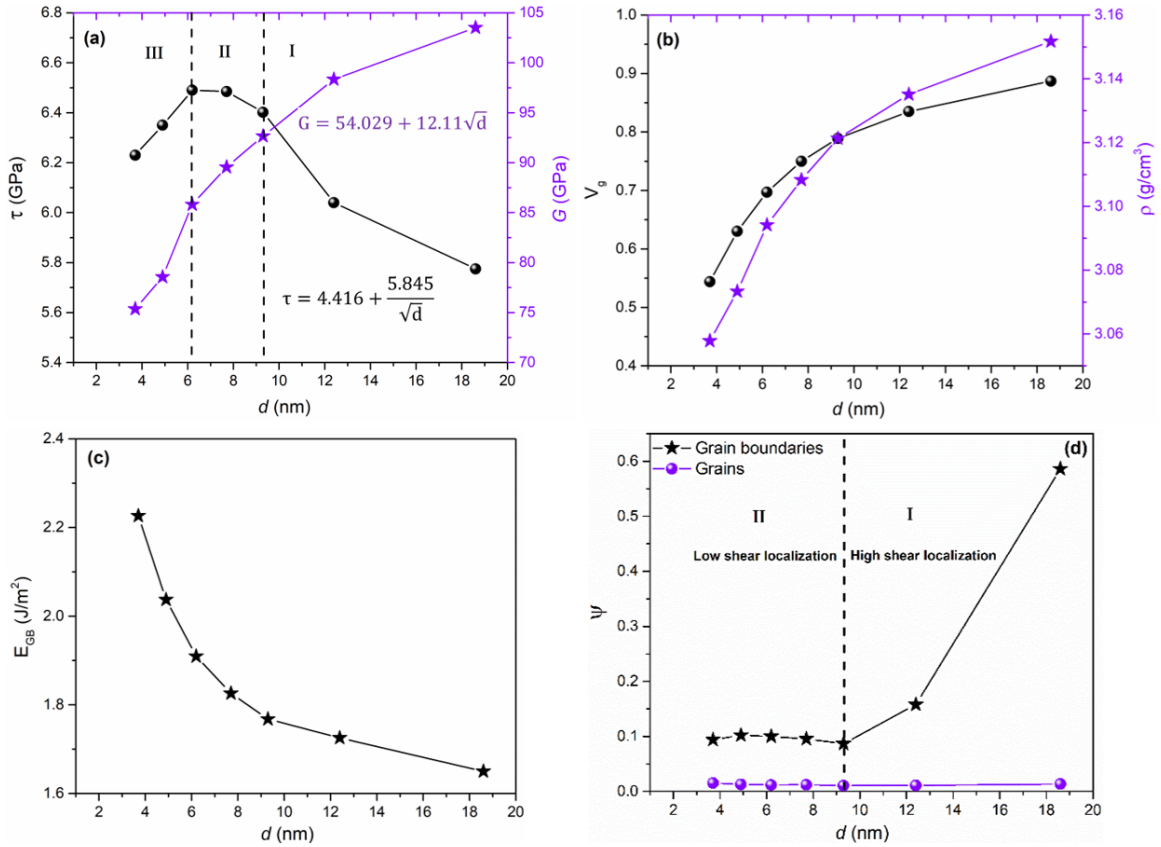

FIG. 3. Grain size dependence of SiC properties. Grain size (d) variation of (a) shear strength (τ) and modulus (G). (b) Crystalline volume fraction (V_g) and density (ρ). (c) Total grain boundary (GB) energy (E_{GB}). (d) Shear localization parameter (Ψ).

TABLE I. Shear properties and density of the 3*C*-SiC crystalline and disordered phases at 300 K.

Shear plane	Shear strength (GPa)	Shear modulus (GPa)	Critical shear strain	Density (g/cm^3)
	Crystalline phase $x[11\bar{2}]$, $y[111]$, $z[\bar{1}10]$ orientation			3.19
xy	14.69	118.34	0.183	
yz	19.97	121.22	0.217	
xz	27.53	125.23	0.259	
	Crystalline phase $x[110]$, $y[\bar{1}10]$, $z[001]$ orientation			
xy	18.11	117.46	0.264	
yz	28.15	128.93	0.256	
xz	28.17	129.14	0.256	
	Crystalline phase $x[100]$, $y[010]$, $z[001]$ orientation			
xy	35.97	129.04	0.327	
yz	35.56	129.08	0.323	
xz	35.98	129.09	0.327	
	Disordered phase			
xy	3.985	37.4	0.205	2.908

have revealed that reduction in GB energy [54–56] can cause strengthening in nanocrystalline metals. On the other hand, higher crystalline volume fraction in a nanocrystalline sample results in higher strength. Note that the disordered structure of the GBs has a lower density, i.e., 2.908 g/cm^3, than the crystalline phase 3.19 g/cm^3, see Table I. Since the nanocrystalline sample is a mixture of both, higher crystalline volume fraction implies a higher density and higher stiffness and strength since the crystalline phase is stiffer and stronger than the amorphous GB phase. In our simulations, it is observed from Fig. 3(c) that the total GB energy decreases with increasing grain size, in agreement with experiments [57], whereas the crystalline volume fraction and density of the samples increase with grain size, as illustrated in Fig. 3(b). It should be mentioned that no dislocation activity, i.e., dislocation nucleation and migration inside grains, is observed during the shear deformation. Shockley partial dislocations in 3*C*-SiC glide in the $\{111\}[11\bar{2}]$ slip system and have a 7.5 GPa Peierls stress [58]. The perfect dislocation-free grain structures and large stresses required to nucleate them, e.g., from GB sources, make dislocation nucleation energetically unfavorable. Thus, dislocation pile-up strengthening, common in metals, is absent in our simulations. It is sensible to assume that total GB energies and crystalline volume fraction of the samples do not play a significant role in shear strengthening response of the nanocrystalline 3*C*-SiC ceramic in the Hall-Petch region, i.e., regions (I) and (II) in Fig. 3(a). Thus, other mechanisms should be responsible for the Hall-Petch behavior displayed.

We evaluated the shear localization behavior in the samples by calculating the shear localization parameter at the yield shear strain point for all the samples considered. As shown in Fig. 3(d), two distinct regions can be identified: (I) high shear localization region for grain sizes >9.3 nm, where tendency for cavitation and intergranular nanocracking and fracture is high, leading to a relatively low strength; (II) low shear localization region for grain sizes <9.3 nm, where shear localization remains nearly constant. Figure 3(d) also shows that the shear strain localizes primarily along GBs, and the grains do not contribute to accommodating the applied shear strain energy; thus, GB-mediated deformation dominates the deformation and failure of 3*C*-SiC at all grain sizes. We assume that shear deformation is more heterogeneous in region (I) shown in Fig. 3(d) owing to the increase in volume fraction of the hard crystalline phase with grain size. During shear deformation, the shear loading energy initially triggers elastic deformation. Larger grain size models in the Hall-Petch regime have a higher crystalline volume fraction, which provides high constraint, leading to the suppression of shear plastic flow and stress relaxation, and generating highly elastically strained regions within GBs. Accordingly, higher elastic energy is stored in larger grain size models. Due to absence of slip systems and nonactive viscous flow within GBs, any further deformation at a critical shear strain energy (or critical stress required to activate local shear events within GBs) linked to the cohesion strength of GBs, is followed by bond breaking, shear localization, GB sliding, cavitation, nanocrack formation [28], and eventually intergranular fracture.

Decrease in grain size is accompanied by the increase in the density of GBs, resulting in delocalization of the overall applied shear stress throughout the structure, minimizing stress concentration along GBs, increasing the shear strength and delocalizing the shear flow, promoting a rather homogeneous shear deformation. However, the strengthening has an inherent threshold as the mechanical properties of very fine-grained nanocrystals become dominated by the properties of the amorphous GB phase [50]. Figure 3(b) indicates that the nanocrystalline ceramics have a total GB volume fraction of ∼0.3 at 6.2 nm grain size. Further grain refinement to 3.7 nm causes an increase in the total GB volume fraction to ∼0.45. Therefore, the shear response of the nanocrystalline ceramic below the Hall-Petch breakdown threshold, region (III), can be associated with the high-volume fraction of the structurally disordered phase within GBs, which makes the sample increasingly soft and weaker. In addition, a conjecture can be posed that the high total GB energy of the fine grain sample, i.e., 3.7 nm grain size, marginally contributes to the weakening and occurrence of an inverse Hall-Petch behavior.

According to the above discussion, we propose the following shear deformation mechanisms for the three regions identified in Fig. 3(a):

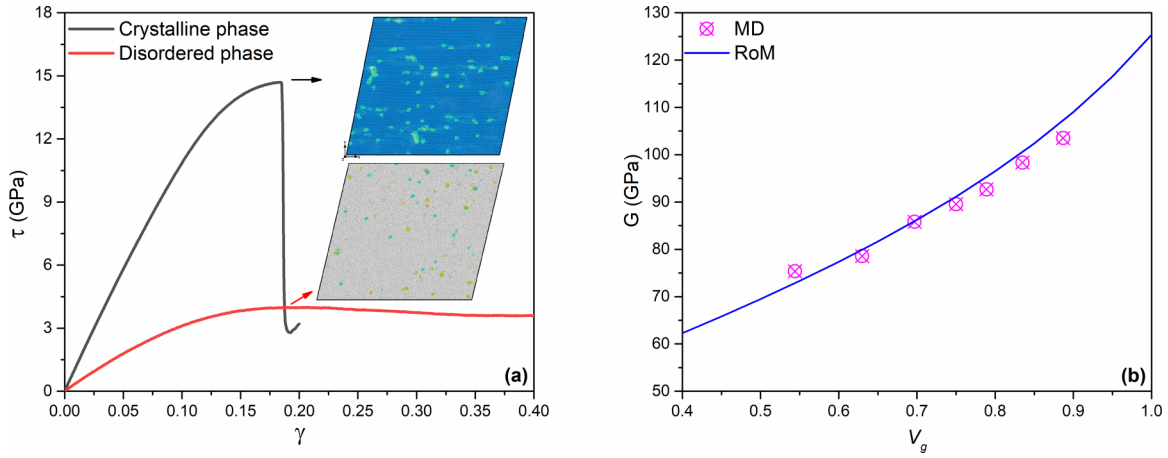

FIG. 4. (a) Shear response of the 3*C*-SiC crystalline and disordered phases at 300 K. The crystalline sample has the directions [11$\bar{2}$], [111], and [$\bar{1}$10] aligned along the *x*, *y*, and *z* axes and is sheared along the *xy* plane. (b) Shear modulus (G) as a function of crystalline volume fraction (V_g) obtained by molecular dynamics (MD) and rule of mixture (RoM).

(i) Grain sizes of 18.6 to 9.3 nm: Strong stress concentration at GBs resulting in shear localization-dominated deformation promoting cavitation and intergranular fracture.

(ii) Grain sizes of 9.3 to 6.2 nm: Stress concentration at GBs minimized due to high density of GBs promoting delocalization of shear stress and homogeneous deformation.

(iii) Grain sizes <6.2 nm: Strong softening effects due to very high-volume fraction of structurally disordered GB phase.

It has been reported that elastic modulus is particularly sensitive to crystalline volume fraction and density of nanocrystalline ceramic [19]. Simulation results shown in Fig. 3(a) indicate that the shear modulus in fact decreases with grain size i.e., from ∼101 GPa (18.6 nm grain size) to ∼71 GPa (3.7 nm grain size). This can be explained directly by the higher crystalline volume fraction of coarser grain samples, as shown in Fig. 3(b). Considering nanocrystalline 3*C*-SiC as a composite, and with the knowledge of the shear modulus of both crystalline and disordered phases, a rule of mixtures (RoM) can be fitted to predict the upper and lower bounds of the shear modulus. Figure 4(a) shows a representative shear stress-strain response of the crystalline and disordered phases. Shear strength, shear modulus, critical shear strain, and density of the crystalline and disordered phases are summarized in Table I. For the crystalline phase, shear properties for the three different crystallographic orientations considered are reported, and the average magnitudes are used in the RoM. Average shear moduli of crystalline and disordered phases are calculated as $G_{\mathrm{Cr}} = 125.28$ GPa and $G_{\mathrm{Dis}} = 37.4$ GPa. Accordingly, the upper- and lower-bound RoMs of shear moduli are defined as

$$G_{\mathrm{UB}}^{\mathrm{RoM}} = 125.28V_g + 37.4(1 - V_g), \tag{1}$$

$$G_{\mathrm{LB}}^{\mathrm{RoM}} = \left(\frac{V_g}{125.28} + \frac{1 - V_g}{37.4}\right)^{-1}. \tag{2}$$

An algebraic average of the upper- and lower-bound RoMs gives

$$G_{\mathrm{average}}^{\mathrm{RoM}} = \frac{G_{\mathrm{UB}}^{\mathrm{RoM}} + G_{\mathrm{LB}}^{\mathrm{RoM}}}{2}. \tag{3}$$

Figure 4(b) illustrates the variation of shear modulus with crystalline volume fraction obtained by MD and the RoM calculations, where an excellent agreement can be observed.

An effort is also made to develop a composite model (CM) to describe the shear strength of the nanocrystalline 3*C*-SiC. In the Hall-Petch regime, shear strength is estimated as

$$\tau = \tau_0 + \frac{k}{\sqrt{d}}, \tag{4}$$

where τ_0 and k are material-dependent constants [2] that can be obtained by fitting to the data in the Hall-Petch regime. The effective shear strength is then calculated using a Hill's-like model [59] $\tau_{\mathrm{average}}^{\mathrm{effective}}$, which is an algebraic average of the upper bound $\tau_{\mathrm{UB}}^{\mathrm{effective}}$ and lower bound $\tau_{\mathrm{LB}}^{\mathrm{effective}}$ of the shear strength:

$$\tau_{\mathrm{average}}^{\mathrm{effective}} = \frac{\tau_{\mathrm{LB}}^{\mathrm{effective}} + \tau_{\mathrm{UB}}^{\mathrm{effective}}}{2}, \tag{5}$$

$$\frac{1}{\tau_{\mathrm{LB}}^{\mathrm{effective}}} = \frac{V_g}{\tau_g} + \frac{V_{gb}}{\tau_{gb}}, \tag{6}$$

$$\tau_{\mathrm{UB}}^{\mathrm{effective}} = V_g\tau_g + V_{gb}\,\tau_{gb}, \tag{7}$$

where V_g, V_{gb}, τ_g, and τ_{gb} represent volume fraction of grains (crystalline volume fraction) and GBs (amorphous interface volume fraction) and shear strength of grains and GBs, respectively [21].

Assuming grains have cubical [60], spherical [60–63], or tetrakaidecahedral [21,64,65] shapes, and denoting d as the average grain size and δ as the GB thickness, the volume fraction of the grain interior for a composite can be approximated by

$$\text{Cubical shape}: V_g = \frac{(d-\delta)^3}{d^3}, \tag{8}$$

$$\text{Spherical shape}: V_g = \frac{(d-\delta)^3}{d^3}\frac{\sqrt{2}\pi}{6}, \tag{9}$$

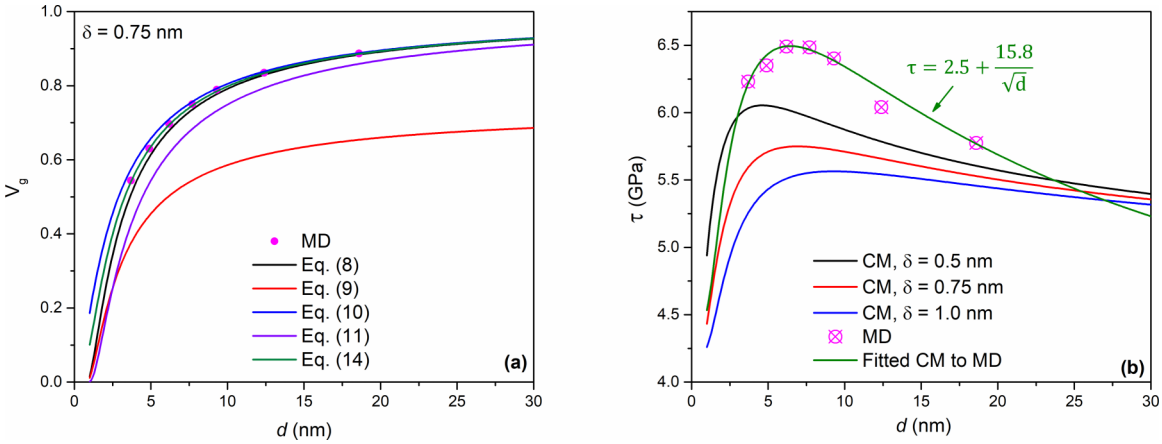

FIG. 5. (a) Comparison of theoretical calculations and molecular dynamics (MD) results for the volume fraction of the grain interior (crystalline volume fraction). (b) Predictions of the theoretical composite model (CM) vs MD results. Fitted CM to MD results are based on $\delta = 1.0$ nm, $\tau_0 = 2.5$ GPa, and $k = 15.8$ GPa nm$^{1/2}$.

or

$$\text{Spherical shape}: V_g = \left(\frac{d}{d+\delta}\right)^3, \tag{10}$$

$$\text{Tetrakaidekahedral shape}: V_g = \left(1 - \frac{3}{\sqrt{6}}\frac{\delta}{d}\right)^3. \tag{11}$$

The structure of real grains, unlike either of these three extremes, could be approximated as a weighted average of two geometries:

$$V_g = \alpha V_{g1} + (1-\alpha)V_{g2}, \tag{12}$$

where α is a weighting factor, which could be related to the volume fraction of GB triple junctions, and the volume fraction of the GBs is

$$V_{gb} = 1 - V_g. \tag{13}$$

Figure 5(a) indicates that both Eqs. (8) and (10) provide better fits to the MD data than other equations, when considering the measured amorphous GB thickness in our models ~0.75 nm. Indeed, the MD data fall between the approximations of Eqs. (8) and (10); thus, a weighted average of two geometries, i.e., cubical and spherical, using Eq. (12) and $\alpha = 0.5$ is employed for the CM:

$$V_g = 0.5\frac{(d-\delta)^3}{d^3} + 0.5\left(\frac{d}{d+\delta}\right)^3. \tag{14}$$

Shear strengths estimated from the CM are plotted in Fig. 5(b) using the material constants $\tau_0 = 4.416$ GPa and $k = 5.845$ GPa nm$^{1/2}$. The GB thickness is varied in the range of 0.5 to 1 nm to explore its probable effect on the estimated shear strength of nanocrystalline 3*C*-SiC. It is worth noting that hydrogen probe studies have demonstrated that the GB thickness is in the range of 0.5 to 1.5 nm [66,67]. In addition, our MD simulations indicate that GB thickness is independent of grain size. As evident from Fig. 5(b), the CM can reasonably predict the shear strength of the nanocrystalline 3*C*-SiC at different grain sizes and the transition between Hall-Petch and inverse Hall-Petch regimes. The critical grain size for the transition between Hall-Petch and inverse Hall-Petch behavior predicted by the CM with $\delta = 0.75$ nm is ~6.3 nm, at a maximum shear strength of ~5.8 GPa, which is in the range of the MD results, i.e., 6.2–7.7 nm. A critical grain size of ~7 nm has recently been reported for a $MgAl_2O_4$ spinel ceramic using a GB sliding activation energy model [68]. The best fit to the MD results, as shown in Fig. 5(b) by the green curve, is obtained with $\delta = 1.0$ nm, $\tau_0 = 2.5$ GPa, and $k = 15.8$ GPa nm$^{1/2}$. An important observation that can be inferred from Fig. 5(b) is the increase of the critical grain size with GB thickness. In addition, in the Hall-Petch regime, the effect of GB thickness on the shear strength is seen to fade away with increasing grain size, which is in accord with the estimates of a micromechanics-based CM for a TiO_2 ceramic [62]. Further analysis indicates that, at a grain size of ~100 nm, GB thickness has almost no impact on the shear strength, see Fig. 6.

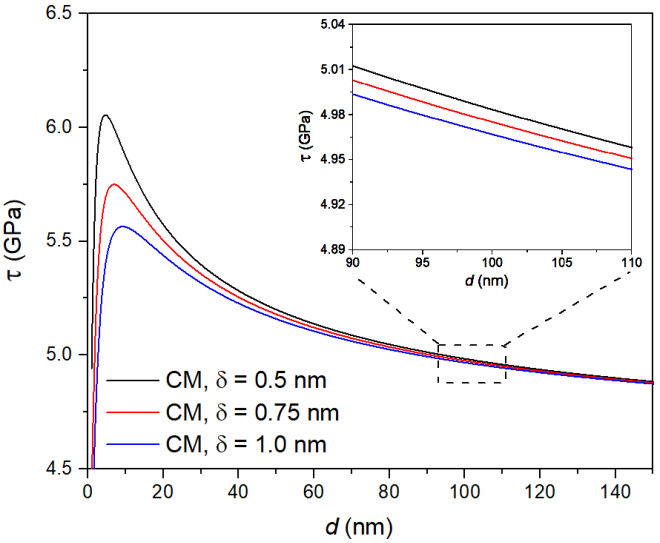

FIG. 6. Diminishing the effect of grain boundary (GB) thickness on shear strength of nanocrystalline 3*C*-SiC at coarse grain range, i.e., ~100 nm.

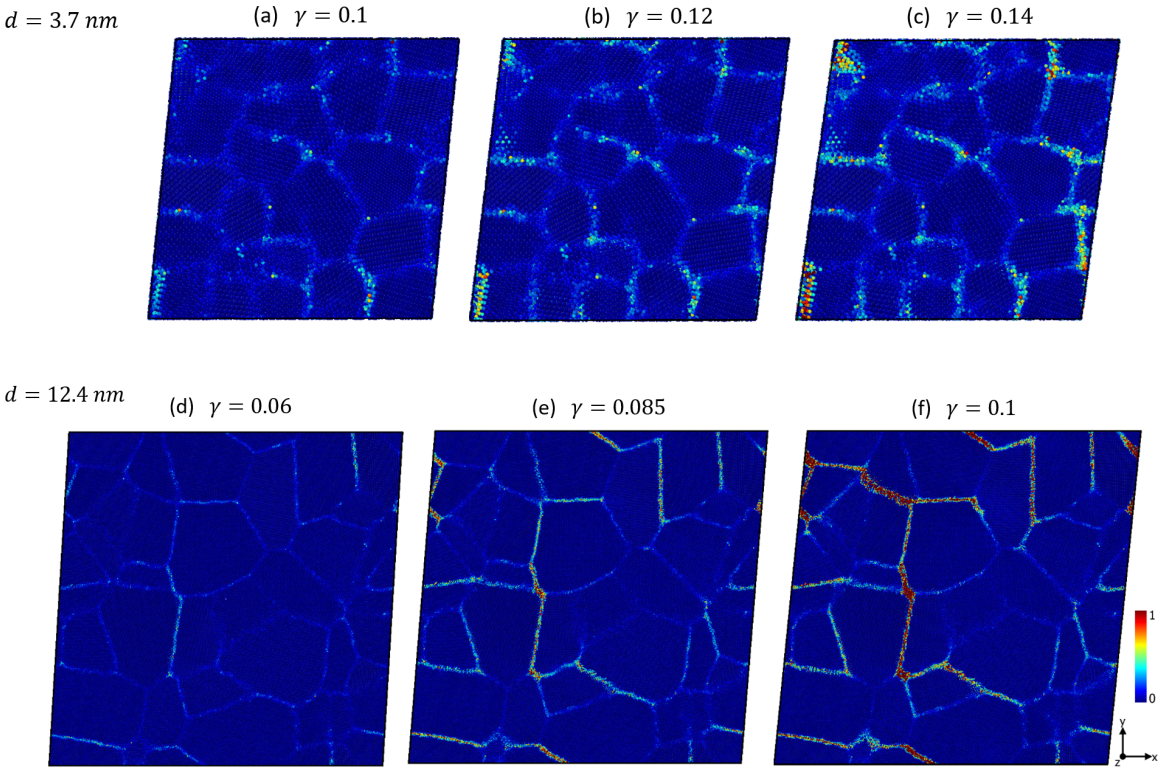

FIG. 7. von Mises local atomic shear strain in the samples with $d = 3.7$ nm and 12.4 nm at different shear strains (γ). Atoms are colored by the von Mises local atomic shear strain proposed by Shimizu *et al.* [51]. Shear localization can be observed within grain boundaries (GBs) in both samples yet with higher extent and magnitudes in the coarser grain sample, triggering the heterogenous deformation.

To further demonstrate the shear localization as well as the homogenous/heterogenous deformation in nanocrystalline 3*C*-SiC, snapshots of two samples with grain sizes of 3.7 and 12.4 nm around the critical shear strains are plotted in Fig. 7, where the atoms are colored by the von Mises local atomic shear strain [51]. We can clearly observe that the atomic shear strain is localized within GBs in all samples. However, the extent and magnitudes of the atomic shear strain are higher in the coarser grain sample, at the point of maximum shear stress, e.g., $\gamma = 0.12$ and 0.085. The results suggest a strong stress concentration at GB and triple junctions for the 12.4 nm grain size, triggering premature failure, resulting in a relatively low strength. In contrast, at the fine grain size of 3.7 nm, the applied shear stress is homogeneously distributed across the sample and minimally intensified at GBs. That delays failure and prompts a rather homogeneous deformation of the sample, resulting in a higher critical shear strain. In all cases, the illustrations of Fig. 7 indicate that the deformation and failure of nanocrystalline 3*C*-SiC is triggered by release of shear strain energy through GB mechanisms, as discussed above and indicated in Fig. 3(d).

Even though the predictions of this paper are well supported and justified, they depend on the quality of the underlying atomistic models based on the Vashishta *et al.* [36] potential interactions. It should be emphasized that the potential for SiC developed by Vashishta *et al.* [36] has been widely validated in many previous studies. A review paper has highlighted some of the most important modeling investigations on SiC nanostructures, including many studies using this potential [69]. As illustrated in Sec. II, the GBs in our models are amorphous. That was also the case in other simulations of nanocrystalline SiC using the same potential, e.g., Refs. [26,27]. Commonly, experimental "as-processed" SiC microcrystalline samples also display amorphous GBs, e.g., Refs. [70,71]. Experimentally, SiC undergoes a pressure-induced structural phase transformation to the rock salt structure at ∼100 GPa. Previous MD simulations using the Vashishta *et al.* [36] potential successfully reported the pressure-induced transformation from the zinc blende to the rock salt structure occurs at ∼90–100 GPa under both hydrostatic and dynamic shock conditions, in excellent agreement with experiments, e.g., Refs. [37,39,72]. The absence of a transformation in this paper is due to the differences in the predominantly shear stress state and the high-pressure conditions required to trigger the structural transformation.

IV. CONCLUSIONS

In this paper, we employed MD simulations to examine the shear deformation behavior of a nanocrystalline 3*C*-SiC ceramic with average grain sizes between 3.7 and 18.6 nm. We found that nanocrystalline 3*C*-SiC exhibits Hall-Petch-like behavior down to grain sizes of 6.2 nm, whereas at finer grain sizes, an observed drop in shear strength indicates a transition into an inverse Hall-Petch regime. In the absence of dislocation activity, the quantitative analysis revealed that the underlying mechanism of the Hall-Petch-like behavior in

3*C*-SiC is rooted in the homogenization of the shear stress across the nanostructure as grain sizes are reduced and GB volume increased. That results in delayed shear localization within GBs preventing cavitation, nanocracking, and premature failure. In contrast, for decreasing grain sizes <6.2 nm, the high-volume fraction of the structurally disordered GB phase, which is rather compliant, play a critical role in the Hall-Petch-like behavior breakdown. The results revealed that shear modulus uniformly decreases as the grain size is reduced from 18.6 to 3.7 nm, demonstrating that the elastic properties of nanocrystalline 3*C*-SiC are directly correlated with the fractions of bulk crystalline and amorphous GB regions. A RoM and a theoretical CM could describe well the shear modulus and shear strength behavior of the nanocrystalline 3*C*-SiC. The findings in this paper provide important insights into the mechanical behavior of nanocrystalline ceramics.

[1] C. Pande and K. Cooper, Nanomechanics of Hall-Petch relationship in nanocrystalline materials, Prog. Mater Sci. **54**, 689 (2009).

[2] Z. Cordero, B. Knight, and C. Schuh, Six decades of the Hall-Petch effect—a survey of grain-size strengthening studies on pure metals, Int. Mater. Rev. **61**, 495 (2016).

[3] M. A. Meyers, A. Mishra, and D. J. Benson, Mechanical properties of nanocrystalline materials, Prog. Mater Sci. **51**, 427 (2006).

[4] J. Schiøtz, F. D. Di Tolla, and K. W. Jacobsen, Softening of nanocrystalline metals at very small grain sizes, Nature **391**, 561 (1998).

[5] S. Xu and S. Z. Chavoshi, Uniaxial deformation of nanotwinned nanotubes in body-centered cubic tungsten, Curr. Appl. Phys. **18**, 114 (2018).

[6] S. Xu, S. Z. Chavoshi, and Y. Su, Deformation mechanisms in nanotwinned tungsten nanopillars: effects of coherent twin boundary spacing, Phys. Stat. Sol. RRL **12**, 1700399 (2018).

[7] S. Z. Chavoshi, M. A. Tschopp, and P. S. Branicio, Transition of deformation mechanisms in nanotwinned single crystalline SiC, Philos. Mag. **99**, 2636 (2019).

[8] S. Z. Chavoshi and S. Xu, Tension-compression asymmetry in plasticity of nanotwinned 3*C*-SiC nanocrystals, J. Appl. Phys. **124**, 095103 (2018).

[9] Q. An and W. A. Goddard, III, Atomistic Origin of Brittle Failure of Boron Carbide from Large-Scale Reactive Dynamics Simulations: Suggestions Toward Improved Ductility, Phys. Rev. Lett. **115**, 105501 (2015).

[10] D. Guo and Q. An, Transgranular amorphous shear band formation in polycrystalline boron carbide, Int. J. Plast. **121**, 218 (2019).

[11] Q. An and W. A. Goddard, III, Nanotwins soften boron-rich boron carbide ($B_{13}C_2$), Appl. Phys. Lett. **110**, 111902 (2017).

[12] S. Z. Chavoshi and S. Xu, Twinning effects in the single/nanocrystalline cubic silicon carbide subjected to nanoindentation loading, Materialia **3**, 304 (2018).

[13] F. Javaid, K. E. Johanns, E. A. Patterson, and K. Durst, Temperature dependence of indentation size effect, dislocation pile-ups, and lattice friction in (001) strontium titanate, J. Am. Ceram. Soc. **101**, 356 (2018).

[14] X. Fang, K. Ding, S. Janocha, C. Minnert, W. Rheinheimer, T. Frömling, K. Durst, A. Nakamura, and J. Rödel, Nanoscale to microscale reversal in room-temperature plasticity in $SrTiO_3$ by tuning defect concentration, Scripta Mater. **188**, 228 (2020).

[15] D. Ghosh, G. Subhash, and G. R. Bourne, Room-temperature dislocation activity during mechanical deformation of polycrystalline ultra-high-temperature ceramics, Scripta Mater. **61**, 1075 (2009).

[16] B. Ratzker, A. Wagner, M. Sokol, L. Meshi, S. Kalabukhov, and N. Frage, Deformation in nanocrystalline ceramics: a microstructural study of $MgAl_2O_4$, Acta Mater. **183**, 137 (2020).

[17] M. Sokol, M. Halabi, Y. Mordekovitz, S. Kalabukhov, S. Hayun, and N. Frage, An inverse Hall-Petch relation in nanocrystalline $MgAl_2O_4$ spinel consolidated by high pressure spark plasma sintering (HPSPS), Scripta Mater. **139**, 159 (2017).

[18] J. A. Wollmershauser, B. N. Feigelson, E. P. Gorzkowski, C. T. Ellis, R. Goswami, S. B. Qadri, J. G. Tischler, F. J. Kub, and R. K. Everett, An extended hardness limit in bulk nanoceramics, Acta Mater. **69**, 9 (2014).

[19] H. Ryou, J. W. Drazin, K. J. Wahl, S. B. Qadri, E. P. Gorzkowski, B. N. Feigelson, and J. A. Wollmershauser, Below the Hall-Petch limit in nanocrystalline ceramics, ACS nano **12**, 3083 (2018).

[20] D. N. Muche, M. A. Marple, I. Hung, Z. Gan, R. H. Castro, and S. Sen, Size-induced structural disorder enables ultrahard oxides, J. Phys. Chem. C **121**, 13898 (2017).

[21] D. Ehre and R. Chaim, Abnormal Hall-Petch behavior in nanocrystalline MgO ceramic, J. Mater. Sci. **43**, 6139 (2008).

[22] Y. Shinoda, T. Nagano, H. Gu, and F. Wakai, Superplasticity of silicon carbide, J. Am. Ceram. Soc. **82**, 2916 (1999).

[23] C. Pan, L. Zhang, W. Jiang, W. Setyawan, L. Chen, Z. Li, N. Liu, and T. Wang, Grain size dependence of hardness in nanocrystalline silicon carbide, J. Eur. Ceram. Soc. **40**, 4396 (2020).

[24] V. Ivashchenko, P. Turchi, and V. Shevchenko, Simulations of the mechanical properties of crystalline, nanocrystalline, and amorphous SiC and Si, Phys. Rev. B **75**, 085209 (2007).

[25] Y. Mo and I. Szlufarska, Simultaneous enhancement of toughness, ductility, and strength of nanocrystalline ceramics at high strain-rates, Appl. Phys. Lett. **90**, 181926 (2007).

[26] J. Zhang, Z. Sha, P. Branicio, Y. Zhang, V. Sorkin, Q. Pei, and D. Srolovitz, Superplastic nanocrystalline ceramics at room temperature and high strain rates, Scripta Mater. **69**, 525 (2013).

[27] I. Szlufarska, A. Nakano, and P. Vashishta, A crossover in the mechanical response of nanocrystalline ceramics, Science **309**, 911 (2005).

[28] D. Guo, S. Song, R. Luo, W. A. Goddard, III, M. Chen, K. M. Reddy, and Q. An, Grain Boundary Sliding and Amorphization are Responsible for the Reverse Hall-Petch Relation in Superhard Nanocrystalline Boron Carbide, Phys. Rev. Lett. **121**, 145504 (2018).

[29] J. Li and S. Yip, Atomistic measures of materials strength, Comput. Model. Eng. Sci. **3**, 219 (2002).

[30] R. Chaim, Percolative composite model for prediction of the properties of nanocrystalline materials, J. Mater. Res. **12**, 1828 (1997).

[31] H. S. Kim and M. B. Bush, The effects of grain size and porosity on the elastic modulus of nanocrystalline materials, Nanostruct. Mater. **11**, 361 (1999).

[32] S. Z. Chavoshi and X. Luo, Atomic-scale characterization of occurring phenomena during hot nanometric cutting of single crystal 3*C*-SiC, RSC Adv. **6**, 71409 (2016).

[33] S. Z. Chavoshi and X. Luo, Molecular dynamics simulation study of deformation mechanisms in 3*C*-SiC during nanometric cutting at elevated temperatures, Mater. Sci. Eng. A **654**, 400 (2016).

[34] P. Mélinon, B. Masenelli, F. Tournus, and A. Perez, Playing with carbon and silicon at the nanoscale, Nat. Mater. **6**, 479 (2007).

[35] S. Plimpton, Fast parallel algorithms for short-range molecular dynamics, J. Comput. Phys. **117**, 1 (1995).

[36] P. Vashishta, R. K. Kalia, A. Nakano, and J. P. Rino, Interaction potential for silicon carbide: a molecular dynamics study of elastic constants and vibrational density of states for crystalline and amorphous silicon carbide, J. Appl. Phys. **101**, 103515 (2007).

[37] W. Li, X. Yao, P. Branicio, X. Zhang, and N. Zhang, Shock-induced spall in single and nanocrystalline SiC, Acta Mater. **140**, 274 (2017).

[38] P. S. Branicio, R. K. Kalia, A. Nakano, and P. Vashishta, Nanoductility induced brittle fracture in shocked high performance ceramics, Appl. Phys. Lett. **97**, 111903 (2010).

[39] P. S. Branicio, J. Zhang, J. P. Rino, A. Nakano, R. K. Kalia, and P. Vashishta, Shock-induced microstructural response of mono- and nanocrystalline SiC ceramics, J. Appl. Phys. **123**, 145902 (2018).

[40] W. Li, E. N. Hahn, X. Yao, T. C. Germann, B. Feng, and X. Zhang, On the grain size dependence of shock responses in nanocrystalline SiC ceramics at high strain rates, Acta Mater. **200**, 632 (2020).

[41] P. S. Branicio, J. Zhang, J. P. Rino, A. Nakano, R. K. Kalia, and P. Vashishta, Plane shock loading on mono- and nanocrystalline silicon carbide, Appl. Phys. Lett. **112**, 111909 (2018).

[42] W. Li, E. N. Hahn, X. Yao, T. C. Germann, and X. Zhang, Shock induced damage and fracture in SiC at elevated temperature and high strain rate, Acta Mater. **167**, 51 (2019).

[43] S. Zhao, R. Flanagan, E. Hahn, B. Kad, B. Remington, C. Wehrenberg, R. Cauble, K. More, and M. Meyers, Shock-induced amorphization in silicon carbide, Acta Mater. **158**, 206 (2018).

[44] H. Tsuzuki, J. Rino, and P. Branicio, Dynamic behaviour of silicon carbide nanowires under high and extreme strain rates: a molecular dynamics study, J. Phys. D **44**, 055405 (2011).

[45] H. Kikuchi, R. K. Kalia, A. Nakano, P. Vashishta, P. S. Branicio, and F. Shimojo, Brittle dynamic fracture of crystalline cubic silicon carbide (3*C*-SiC) via molecular dynamics simulation, J. Appl. Phys. **98**, 103524 (2005).

[46] J. P. Rino, I. Ebbsjö, P. S. Branicio, R. K. Kalia, A. Nakano, F. Shimojo, and P. Vashishta, Short-and intermediate-range structural correlations in amorphous silicon carbide: a molecular dynamics study, Phys. Rev. B **70**, 045207 (2004).

[47] G. Voronoi, New applications of continuous parameters in the theory of quadratic forms, Z. Reine Angew. Math **133**, 97 (1908).

[48] E. Maras, O. Trushin, A. Stukowski, T. Ala-Nissila, and H. Jonsson, Global transition path search for dislocation formation in Ge on Si (001), Comput. Phys. Commun. **205**, 13 (2016).

[49] See Supplemental Material at http://link.aps.org/supplemental/10.1103/PhysRevMaterials.5.073606 for the grain size distribution of nanocrystalline 3*C*-SiC samples and reproducibility of the results.

[50] T. Brink and K. Albe, From metallic glasses to nanocrystals: molecular dynamics simulations on the crossover from glass-like to grain-boundary-mediated deformation behaviour, Acta Mater. **156**, 205 (2018).

[51] F. Shimizu, S. Ogata, and J. Li, Theory of shear banding in metallic glasses and molecular dynamics calculations, Mater. Trans. **48**, 2923 (2007).

[52] S. Z. Chavoshi, S. Goel, and X. Luo, Influence of temperature on the anisotropic cutting behaviour of single crystal silicon: a molecular dynamics simulation investigation, J. Manuf. Processes **23**, 201 (2016).

[53] A. Stukowski, Computational analysis methods in atomistic modeling of crystals, JOM **66**, 399 (2014).

[54] N. Q. Vo, R. S. Averback, P. Bellon, and A. Caro, Yield strength in nanocrystalline Cu during high strain rate deformation, Scripta Mater. **61**, 76 (2009).

[55] A. v. Hasnaoui, H. Van Swygenhoven, and P. Derlet, On non-equilibrium grain boundaries and their effect on thermal and mechanical behaviour: a molecular dynamics computer simulation, Acta Mater. **50**, 3927 (2002).

[56] N. Q. Vo, R. S. Averback, P. Bellon, and A. Caro, Limits of hardness at the nanoscale: molecular dynamics simulations, Phys. Rev. B **78**, 241402(R) (2008).

[57] D. N. Muche, M. A. Marple, S. Sen, and R. H. Castro, Grain boundary energy, disordering energy and grain growth kinetics in nanocrystalline $MgAl_2O_4$ spinel, Acta Mater. **149**, 302 (2018).

[58] H.-P. Chen, R. K. Kalia, A. Nakano, P. Vashishta, and I. Szlufarska, Multimillion-atom nanoindentation simulation of crystalline silicon carbide: orientation dependence and anisotropic pileup, J. Appl. Phys. **102**, 063514 (2007).

[59] R. Hill, The elastic behaviour of a crystalline aggregate, Proc. Phys. Soc. **65**, 349 (1952).

[60] J. Carsley, J. Ning, W. Milligan, S. Hackney, and E. Aifantis, A simple, mixtures-based model for the grain size dependence of strength in nanophase metals, Nanostruct. Mater. **5**, 441 (1995).

[61] B. Jiang and G. Weng, A composite model for the grain-size dependence of yield stress of nanograined materials, Metall. Mater. Trans. A **34**, 765 (2003).

[62] B. Jiang and G. Weng, A theory of compressive yield strength of nano-grained ceramics, Int. J. Plast. **20**, 2007 (2004).

[63] L. Capolungo, M. Cherkaoui, and J. Qu, On the elastic-viscoplastic behavior of nanocrystalline materials, Int. J. Plast. **23**, 561 (2007).

[64] G. Palumbo, S. J. Thorpe, and K. T. Aust, On the contribution of triple junctions to the structure and properties of nanocrystalline materials, Scripta Meta **24**, 1347 (1990).

[65] R. Chaim, Plastic deformation in impure nanocrystalline ceramics, J. Mater. Res. **14**, 2508 (1999).

[66] T. Mütschele and R. Kirchheim, Hydrogen as a probe for the average thickness of a grain boundary, Scripta Meta **21**, 1101 (1987).

[67] R. Kirchheim, T. Mütschele, W. Kieninger, H. Gleiter, R. Birringer, and T. Koble, Hydrogen in amorphous and nanocrystalline metals, Mater. Sci. Eng. **99**, 457 (1988).

[68] A. G. Sheinerman, R. H. Castro, and M. Y. Gutkin, A model for direct and inverse Hall-Petch relation for nanocrystalline ceramics, Mater. Lett. **260**, 126886 (2020).

[69] P. S. Branicio, Atomistic mechanisms in silicon carbide nanostructures, J. Comput. Theor. Nanosci. **9**, 1870 (2012).

[70] K. Biswas, Solid state sintering of SiC-ceramics, Mater. Sci. Forum **624**, 71 (2009).

[71] D. Chen, X.-F. Zhang, and R. O. Ritchie, Effects of grain-boundary structure on the strength, toughness, and cyclic-fatigue properties of a monolithic silicon carbide, J. Am. Ceram. Soc. **83**, 2079 (2000).

[72] F. Shimojo, I. Ebbsjö, R. K. Kalia, A. Nakano, J. P. Rino, and P. Vashishta, Molecular Dynamics Simulation of Structural Transformation in Silicon Carbide Under Pressure, Phys. Rev. Lett. **84**, 3338 (2000).